AGU PUBLICATIONS

JGR

Journal of Geophysical Research: Earth Surface

RESEARCH ARTICLE
10.1002/2016JF004060

Key Points:
- Dynamic fragmentation occurs in rapid rock mass movements due to shearing of highly stressed grain chains and extremely rapid loadings
- Fragmentation-induced momentum boost is capable of enhancing the fragment impulsive velocity and thus increases its mobility
- The rock damage ratio, fracture stress, nominal size, and fragment number all increase with the applied impact loading strain rate

Supporting Information:
- Supporting Information S1

Correspondence to:
T. Zhao,
zhaotao@scu.edu.cn

Citation:
Zhao, T., G. B. Crosta, S. Utili, and F. V. De Blasio (2017), Investigation of rock fragmentation during rockfalls and rock avalanches via 3-D discrete element analyses, *J. Geophys. Res. Earth Surf.*, *122*, 678–695, doi:10.1002/2016JF004060.

Received 21 OCT 2016
Accepted 2 MAR 2017
Accepted article online 6 MAR 2017
Published online 23 MAR 2017

The copyright line for this article was changed on 30 MAR 2017 after original online publication

Investigation of rock fragmentation during rockfalls and rock avalanches via 3-D discrete element analyses

Tao Zhao[1,2], Giovanni Battista Crosta[3], Stefano Utili[4], and Fabio Vittorio De Blasio[3]

[1]State Key Laboratory of Hydraulics and Mountain River Engineering, College of Water Resource and Hydropower, Sichuan University, Chengdu, China, [2]State Key Laboratory of Geohazard Prevention and Geoenvironment Protection, Chengdu University of Technology, Chengdu, China, [3]Department of Earth and Environmental Sciences, Università degli Studi di Milano Bicocca, Milan, Italy, [4]School of Civil Engineering and Geosciences, Newcastle University, Newcastle upon Tyne, UK

Abstract This paper investigates the characteristics of dynamic rock fragmentation and its influence on the postfailure fragment trajectory. A series of numerical simulations by discrete element method (DEM) were performed for a simple rock block and slope geometry, where a particle agglomerate of prismatic shape is released along a sliding plane and subsequently collides onto a flat horizontal plane at a sharp kink point. The rock block is modeled as an assembly of bonded spherical particles with fragmentation arising from bond breakages. Bond strength and stiffness were calibrated against available experimental data. We analyzed how dynamic fragmentation occurs at impact, together with the generated fragment size distributions and consequently their runout for different slope topographies. It emerges that after impact, the vertical momentum of the granular system decreases sharply to nil, while the horizontal momentum increases suddenly and then decreases. The sudden boost of horizontal momentum can effectively facilitate the transport of fragments along the bottom floor. The rock fragmentation intensity is associated with the input energy and increases quickly with the slope angle. Gentle slopes normally lead to long spreading distance and large fragments, while steep slopes lead to high momentum boosts and impact forces, with efficient rock fragmentation and fine deposits. The fragment size decreases, while the fracture stress and fragment number both increase with the impact loading strain rate, supporting the experimental observations. The fragment size distributions can be well fitted by the Weibull's distribution function.

Plain Language Summary Fragmentation occurring in rapid rock mass movements due to shearing of highly stressed grain chains and extremely rapid loading could be described as dynamic fragmentation. In this study, we present a series of simulations by discrete element method for a simple block and slope geometry, where a particle agglomerate of prismatic shape is released along a sliding plane and subsequently collides onto a flat horizontal plane at a sharp kink point. The fragmentation is intense in the lower frontal part of the rock block, whereas the upper part suffers little from impact, generating relatively large fragments. The sudden impact causes the major damage of rock mass, whereas subsequent sliding and collision lead to further rock fragmentation. At impact, the vertical velocity decreases, while the horizontal velocity increases sharply, facilitating the transport of fragments along the bottom floor. The slope angle influences rock fragmentation by controlling the momentum distribution in the sliding and colliding processes. Gentle slopes normally lead to long spreading distance and large fragments, while steep slopes lead to high momentum boosts and impact forces, with efficient rock fragmentation and finer deposits. The role of strain rate on the degree of fragmentation is studied, and numerical results support the experimental observations.

1. Introduction

Rockslides, rockfalls, and rock avalanches can be associated with almost instantaneous collapse and spreading [*Heim*, 1882; *Scheidegger*, 1973; *Erismann and Abele*, 2001; *Legros*, 2002; *Crosta et al*., 2007; *De Blasio and Crosta*, 2015]. They pose significant hazards to human lives, structures and infrastructures, and lifeline facilities worldwide due to their high mobility, threatening populated areas located even far away from the slope source [*Whitehouse and Griffiths*, 1983; *Stoopes and Sheridan*, 1992; *Crosta et al*., 2005; *Hermanns et al*., 2013; *Zhou et al*., 2013]. These natural disasters have been a subject of intensive research due to their significant destructive power.

Rock avalanches exhibit a still unexplained mechanism of long travel distances [*Erismann and Abele*, 2001]. The mobility can be quantified by the apparent friction coefficient of the so-called "Fahrböschung" [*Scheidegger*, 1973], defined as the ratio between the drop height, H, to the spreading length, L [*Corominas*, 1996].

Based on these two parameters, the Fahrböschung angle, α, can be defined as $\tan^{-1}(H/L)$ [*Shreve*, 1968], and a low traveling angle indicates a highly mobile rock avalanche. As stated by *Bowman et al*. [2012] and *Legros* [2002], the Fahrböschung angle incorporates the effect of rock spreading. Generally, the value of *H*/*L* decreases with the rock avalanche volume, indicating that large rock avalanches exhibit high spreading efficiency. For instance, large rockslides-avalanches on Earth can have volumes of 10^7–10^{11} m^3 and areal spreading of up to 1000 km^2 [*Bowman et al*., 2012]. Since the solid mass would gradually deposit at the base of the sliding path, avalanches progressively run out of material. Thus, the mobility of rockslides beyond a certain location should depend primarily on the solid volume passing through that location, rather than the total rockslide volume [*Legros*, 2002]. However, for small-scale rockfalls (with volumes less than 10^5 m^3) and some laboratory tests, the *H*/*L* ratio only obeys a simple Coulomb frictional law [*Hutter et al*., 1995].

In the literature, many hypotheses have been proposed to explain the apparent high mobility of large rock avalanches, including basal rock melting [*Erismann and Abele*, 2001; *De Blasio and Elverhøi*, 2008], sand fluidization [*Hungr and Evans*, 2004], destabilization of loose masses along the failure plane [*Iverson et al*., 2011], acoustic fluidization [*Collins and Melosh*, 2003], pore fluids such as water [*Legros*, 2002; *De Blasio*, 2009] or vapor [*Habib*, 1975; *Goguel*, 1978; *De Blasio*, 2007], or grain segregation-induced friction decrease [*Phillips et al*., 2006; *Linares-Guerrero et al*., 2007]. Though some of the invoked mechanisms may be important for some specific events, none of them has been acknowledged as a universal explanation for rock avalanche mobility. Site investigations show that the deposits of long runout rock avalanches are intensely fragmented; thus, "dynamic fragmentation" has been proposed as a possible mechanism governing rock avalanche mobilization [*Davies and McSaveney*, 1999; *Locat et al*., 2006]. Some authors proposed this process as a mechanism affecting rock avalanche runout [*Calvetti et al*., 2000; *De Blasio and Crosta*, 2014; *De Blasio and Crosta*, 2015], while others sought to characterize the grain size distribution of fragments and the involved energy losses, both through observations in real rock avalanche deposits [*Dunning*, 2006; *Locat et al*., 2006; *Strom*, 2006; *Crosta et al*., 2007] and physical models [*Imre et al*., 2010; *Bowman et al*., 2012; *Haug et al*., 2016]. *Davies and McSaveney* [1999] investigated the avalanching of dry sands and gravels in laboratory scale experiments. They observed that fragmented rock avalanches can normally have much greater longitudinal spreading distance than nonfragmented ones. This process involves an increase in fragment number and rockfall energy loss, affecting both the fragment trajectory and runout [*Agliardi and Crosta*, 2003; *Ruiz-Carulla et al*., 2016]. So far, the impact-induced fragmentation of a rock mass is still poorly understood.

For numerical modeling of rock avalanches, the discrete element method (DEM) [*Cundall and Strack*, 1979] has been widely used [*Calvetti et al*., 2000; *Taboada and Estrada*, 2009; *Boon et al*., 2014, 2015; *Zhao et al*., 2016, 2017]. *De Blasio and Crosta* [2015] employed a simple 2-D DEM model to study the fragmentation behavior of rock mass along a slope break profile. They suggested that for slope angles greater than 70°, the fragmentation process can produce uniformly distributed fragments, with significantly enhanced momentum and runout distance. Because of the extremely fast loading rate occurring during many rock avalanche events, it is important to mention the role of strain rate at controlling rock strength [*Okubo et al*., 2006] and fracture nucleation [*Grady*, 1981; *Grady and Kipp*, 1985]. Generally, the compressive strength of rock increases with the loading strain rate [*Li and Xia*, 2000; *Fuenkajorn and Kenkhunthod*, 2010; *Wang et al*., 2013]. If the loading is sufficiently rapid, brittle particle agglomerates can be dynamically fragmented [*Rait et al*., 2012]. *Zhao et al*. [2014] performed experimental and numerical investigations of the failure behavior of brittle coal under uniaxial compression for various loading strain rates. They reported that the strength and failure mechanisms of a coal rock mass depend on the loading strain rate and also the microstructure of the material.

Recently, at least two experimental studies investigated the fragmentation of a small brittle block, sliding along a plane, against a slope break [*Bowman et al*., 2012; *Haug et al*., 2016]. Although fragmentation of a rock avalanche is far more severe than shown by experiments (volumetric ratios between the original total rock volume and fine products may exceed 10^{18} [*De Blasio and Crosta*, 2014]) and more complex in its physical description, the experimental situation considered by *Bowman et al*. [2012] and *Haug et al*. [2016] constitutes a reasonable initial proxy to study fragmentation and propagation [*De Blasio and Crosta*, 2015]. Thus, in this work we will consider this setting for our numerical simulations. The primary aim here is to investigate the characteristics of dynamic rock fragmentation and the mechanism governing the postfailure fragment trajectory motions by numerically simulating experiments of rock blocks subject to single impact. The paper is

organized as follows: in section 2, the DEM theory of bonded particle model is illustrated. In section 3, the obtained numerical results of rock avalanche and fragmentation are presented. Section 4 presents the discussions of some issues of rock fragmentation, such as lateral confinement of rock avalanche, spreading mobility, and impact-induced energy dissipation. Finally, some conclusions on the capability of the DEM to model rock fragmentations are provided.

2. DEM Bonded Particle Model

The open source DEM code ESyS-Particle [*Weatherley et al*., 2011] was employed to run all the simulations presented herein. In the DEM model, the brittle rock mass was simulated as an assembly of particles cemented together via the so-called parallel bond model [*Itasca*, 2003; *Potyondy and Cundall*, 2004]. The interactions between bonded particles are calculated as

$$F_{\mathrm{bn}} = K_{\mathrm{bn}} \cdot (I - I_0) \tag{1}$$

$$F_{\mathrm{bs}} = K_{\mathrm{bs}} \cdot \Delta u_s \tag{2}$$

$$M_b = K_b \cdot \Delta\alpha_b \qquad M_t = K_t \cdot \Delta\alpha_t \tag{3}$$

where F_{bn}, F_{bs} are the normal and shear bonding forces; M_b and M_t are the bending and twisting moments, respectively; K_{bn}, K_{bs}, K_b, and K_t are the corresponding bonding stiffness in the normal, shear, bending, and twisting directions, and Δu_s, $\Delta\alpha_b$, and $\Delta\alpha_t$ are the relative displacements between bonded particles in the shear, bending, and twisting directions, calculated via the quaternion based 3-D rigid body spatial rotations [*Wang*, 2009]. I and I_0 are the current and initial distances between particle centers. Note that the initial distance between particles is the distance prior to the motion onset.

In the DEM model, the bonding stiffness can be calculated as $K_{\mathrm{bn}} = \pi E_b I_0/4$, $K_{\mathrm{bs}} = \pi E_b I_0/(8(1+\nu))$, $K_b = \pi E_b I_0^3/64$, and $K_t = \pi E_b I_0^3/(64(1+\nu))$ with E_b being the bond Young's modulus and v being the Poisson's ratio [*Wang et al*., 2006; *Wang*, 2009]. Bond breakages are assumed to be brittle, i.e., as soon as the bond strength capacity is exceeded, it breaks [*Wang et al*., 2006; *Wang*, 2009; *Weatherley et al*., 2011]. The following failure criterion is used to determine whether a bond breaks

$$\frac{F_{\mathrm{bn}}}{F_{\mathrm{bnMax}}} + \frac{F_{\mathrm{bs}}}{F_{\mathrm{bsMax}}} + \frac{M_b}{M_{b\mathrm{Max}}} + \frac{M_t}{M_{t\mathrm{Max}}} \geq 1 \tag{4}$$

where F_{bnMax} and F_{bsMax} are the maximum normal and shear forces respectively; M_{bMax} and M_{tMax} are the maximum bending and twisting moments of interparticle bonds, respectively. They can be evaluated as $F_{\mathrm{bnMax}} = \pi c I_0^2/(4\tan(\phi))$, $F_{\mathrm{bsMax}} = \pi c I_0^2/4$, $M_{b\mathrm{Max}} = \pi c I_0^3/(32\tan(\phi))$, and $M_{t\mathrm{Max}} = \pi c I_0^3/16$, with c and ϕ being the cohesion and internal friction angle of the bond material, respectively.

After breakage, the dispersed particles interact with each other via a linear-elastic spring contact model

$$F_n = K_n \cdot u_n \tag{5}$$

$$F_s^i = F_s^{i-1} + K_s \cdot \Delta u_s \tag{6}$$

where F_n, K_n, and u_n are the normal contact force, stiffness, and overlapping distance between two particles in contact; F_s^i and F_s^{i-1} are the shear forces calculated at the current and previous simulation time steps, respectively; K_s is the shear stiffness; and Δu_s is the incremental shear displacement. In the model, the values of K_n and K_s are calculated as $K_n = \pi E\overline{R}/2$ and $K_s = \pi E\overline{R}/(4(1+\nu))$, with $\overline{R}$ and E being the mean particle radius and Young's modulus, respectively. In addition, viscous damping, proportional to the relative velocities of the particles in contact, is employed to replicate the energy dissipated by particle asperities being sheared off and the plastic deformations of the contacting particles occurring in the vicinity of the points where they are in contact with adjacent particles. Note that rigor viscous damping (the restitution coefficient) is a function of the number of impacts [*Murugaratnam et al*., 2015], but here a constant coefficient has been assumed for the sake of simplicity. The maximum shear force is limited by a frictional slider ($F_{s,\max} = \mu F_n$, with μ being the friction coefficient). Detailed numerical scheme of explicit integration for particle motion in DEM simulations can be found in *Potyondy and Cundall* [2004].

The DEM bonded particle model used in this study was calibrated via 3-D numerical uniaxial compression strength (UCS) tests for quasi-static loading conditions and Split-Hopkinson Pressure Bar (SHPB) tests for dynamic loading conditions on intact rock samples [*Yoon*, 2007; *Shimizu et al*., 2010; *Wang and Tonon*, 2011].

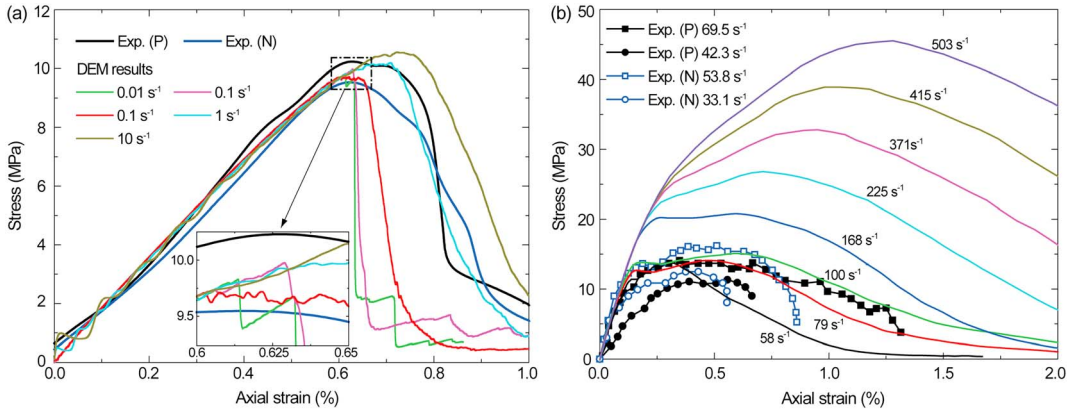

Figure 1. DEM results of (a) 3-D unconfined uniaxial compression tests and (b) Split-Hopkinson Pressure Bar (SHPB) tests on coal rock specimens. In the figure, "Exp.(P)" and "Exp.(N)" stand for experimental data on coal rock with bedding parallel and normal to the loading direction, respectively.

Due to insufficient mechanical characterization of the coal material used in the rock avalanche experiments by *Bowman et al*. [2012], we calibrated the DEM parameters against the available static and dynamic tests on parallel and normal bedding coal samples in *Liu et al*. [2015] (see the notations Exp. (P) and Exp. (N) in Figure 1). For the static UCS tests, the loading strain rate ($\dot{\varepsilon}$) is set between 0.01 and 10 s^{-1}. Further decrease of strain rate would significantly increase the computational cost (e.g., for the case of $\dot{\varepsilon} = 0.01\ s^{-1}$, 7 days on an Intel® Core™ i7 CPU, 4.00 GHz × 8, and 16 GB RAM desktop computer). The configuration of the numerical SHPB test is taken from *Xu et al*. [2016]. The input parameter values of the simulations were selected by trial and error (see Table 1), to ensure the overall shear strength and deformation of the coal rock specimen can match experimental results.

Figure 1a shows the comparison between the numerical results of this study and experimental data on coal rock samples by *Liu et al*. [2015]. The peak shear strength (τ_{peak}) of the coal rock increases with the loading rate, whereas the Young's modulus (E) is unaffected. For tests with strain rate smaller than 1 s^{-1}, the stress-strain relationships are approximately the same before failure, indicating that the quasi-static state condition is satisfied. In these tests, τ_{peak} and E are 9.8 MPa and 1.67 GPa, respectively, which can match well the experimental data. At failure, the DEM rock specimens loaded at small strain rates (e.g., 0.01 $s^{-1}$and 0.1 s^{-1}) behave in a brittle fashion, while they show a more ductile behavior at larger strain rates (e.g., 1 s^{-1}, 5 s^{-1}, and 10 s^{-1}), with a gradual increase of strength. At high loading rate (e.g., to 5 s^{-1} and 10 s^{-1}), the stress-strain curves manifest clear oscillations in the initial loading stage due to stress wave reflections at the loading platens. This effect becomes especially evident at increasing loading rates [*Wang and Tonon*, 2011]. For the results of dynamic SHPB tests in Figure 1b, both the peak strength and the corresponding deformation increase with the loading rate, while the initial shear elastic modulus remains constant, qualitatively matching experimental results by *Liu et al*. [2015] (e.g., for $\dot{\varepsilon} < 100\ s^{-1}$). According to the DEM simulations run at small loading rates ($\leq 100\ s^{-1}$), the peak strength remains almost unaltered (13 MPa), while for higher loading rates ($> 100\ s^{-1}$), both the peak strength and the corresponding strain increase significantly (see also Figure S1 in the supporting information).

Table 1. Input Parameters of the Calibrated DEM Model Built for the Simulation of UCS and Split-Hopkinson Pressure Bar (SHPB) Tests

DEM Parameters	Value	DEM Parameters	Value
Particle radius, r (mm)	[0.75, 2.25]	Young's modulus of bond, E_b (GPa)	1.25
No. of particles, N	18,800	Cohesion of bonds, c (MPa)	14.25
Density, ρ (kg/m^3)	2,650	Viscous damping coefficient, β	0.01
Particle friction angle, φ(deg)	30	Gravitational acceleration, g (m/s^2)	0.0
Particle Poisson ratio, υ	0.25	Packing porosity, n	0.41
Young's modulus of particle, E (GPa)	5	DEM time step, Δt (s)	10^{-7}

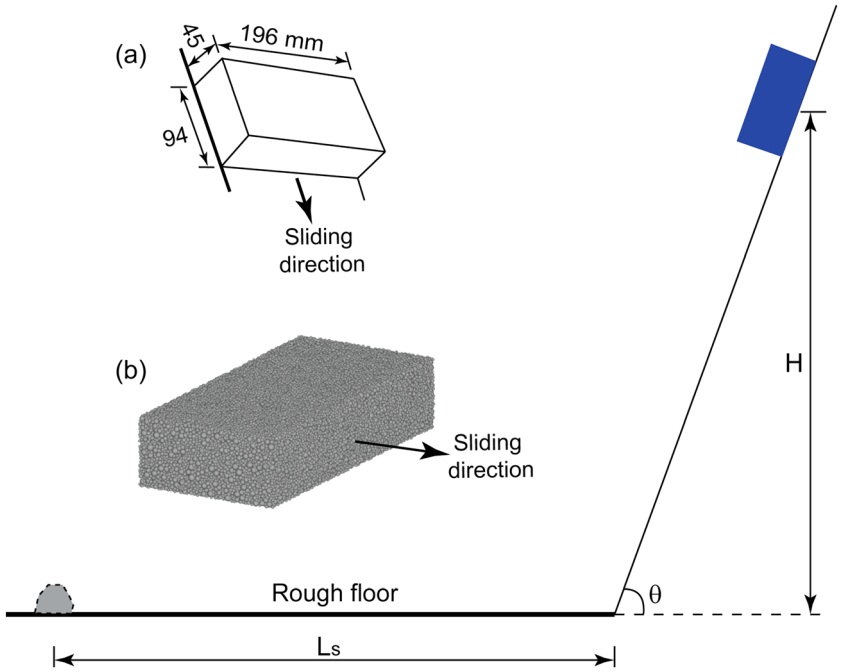

Figure 2. Geometry of physical model adopted for investigating rock fragmentation in rock avalanches by *Bowman et al.* [2012] and *Haug et al.* [2016] (H is the initial block height. θ is the slope angle. L_s is the runout distance of the most distal fragment made of at least 10 particles). The (a) geometry and the (b) DEM representation of the sliding block are shown.

3. DEM Simulation of a Rock Block Fragmentation

A schematic view of rock mass releasing along a steep inclined sliding plane and colliding onto a flat horizontal plane at a sharp break is shown in Figure 2. The rock block simulated in our DEM tests is made of 78,327 densely packed particles and bonded together by breakable parallel bonds of assigned strength. The width of the sliding channel is slightly larger than the width of the granular block, so that the rock mass can slide downslope without touching the side walls. The sliding slope consists of a frictionless rigid wall, with the height (H) of 425 mm, while the horizontal floor of a layer of fixed particles mimicking a rough plane. The slope angle was varied from 40° to 90° to simulate different topographic conditions. An enhanced gravitational acceleration of 1962 m/s^2 (200 g) is applied in each set of simulations to mimic the centrifuge loading. The model configuration is similar to the experimental setup employed in *Bowman et al.* [2012], made of coal blocks or powder in a centrifuge apparatus to increase gravity, and *Haug et al.* [2016], made of a mixture of sand with gypsum-anhydrite or potato starch in a 1 g model. Each block was released from the top of a steep slope and runout onto a horizontal plane. Though only one breakage "step" can be modeled in this configuration, it is assumed that the current study can capture the important characteristics of dynamic rock fragmentation and subsequently reveal the link between rock avalanche fragmentation and mobilization.

3.1. Fragmentation of an Intact Rock Block

In this section, the general features of the fragmentation process taking place in an initially intact coal rock block released on a straight slope of 70° inclination are illustrated. In the following analyses, nondimensional parameters are used (e.g., the normalized sliding time is defined as $[T] = t/\sqrt{2H/g}$), in order to generalize the results of our numerical simulations to rock avalanches of different geometry [*Utili et al.*, 2015].

Figure 3 shows the sliding and fragmentation processes undergone by the rock block following its impact with the horizontal plane. The algorithm used to track each generated fragment is provided in the supporting information of the paper. For visualization purpose, fragments were colored with a set of distinct colors, while single dispersed particles are plotted in light grey. A series of tick marks 1 cm apart are plotted on both sides of the flow path on the graphs for ease of identification of the distance traveled by the fragments. The

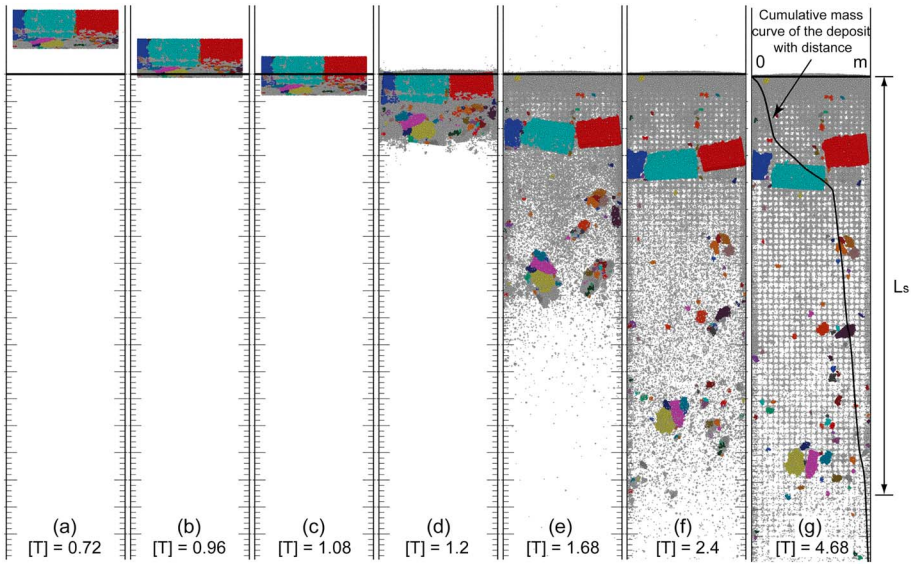

Figure 3. (a–g) Plan view of the motion of rock fragments for an intact rock block at different time. The initial velocity of rock block is 0 m/s, and the impact velocity at the slope break is 40.5 m/s. Grey dots represent dispersed granular particles, and the bold black line on the top region represents the slope break. In Figure 3g, the mass accumulation along the spreading path is plotted as a cumulative mass curve. The runout distance is L_s, time is normalized as $t/\sqrt{2H/g}$, and slope $\theta = 70°$.

horizontal bold black lines plotted on the top of these graphs represent the slope break. It can be observed that rock fragmentation occurs immediately after the block collides with the bottom floor, which is followed by horizontal spreading of fragments. Lateral dispersion of fragments can also be observed from $[T] = 1.08$ to $[T] = 1.2$, from volume dilation occurring after impact. However, the lateral motion of granular material was constrained by the side walls of the channel under the current model configuration. The lateral dispersion caused by rock fragmentation will be discussed in section 4 of this paper. In the final deposit (i.e., at $[T] = 4.68$), the major portion of the highly fragmented rock mass (e.g., dispersed particles) deposits near the slope toe, while relatively large rock fragments can move a long distance on the floor. The final runout distance of the most distal fragment is labeled as L_s in the figure, further to which the dispersed particles amount to around 4% of the total rock block mass. On the plots, the presence of dispersed particles in the final granular deposit makes the calculation of L_s a nonstraightforward exercise. In this study, L_s is measured as the displacement of the mass center of the most distal fragment consisting of at least 10 particles, so ignoring the occasional saltating particles running ahead of the front. The accumulative mass curve of the fragments in the final static deposit is plotted in Figure 3g, with the leftmost point representing the zero mass (i.e., deposit initiation) and the rightmost point representing the total rock block mass. Looking at the curve, it exhibits sharp increases at the location where large fragments were come to rest.

According to *De Blasio and Crosta* [2015], short-lived force chains within the impacting block control its fragmentation behavior, because particle agglomerates associated to dominant force chains are subjected to intense compression and are most likely to break [*McDowell and Bolton*, 1998]. In Figure 4, the total forces, defined as the summation of normal particle contact and bonding forces, are plotted with the line thickness being proportional to the force magnitude (see Figures 4a1–4a5). In addition, the evolution of bonding force chains is plotted in Figures 4b1–4b5. It can be observed that before impact the force chains are uniformly distributed within the rock mass, with the force magnitude smaller than 50 N. At impact (see Figure 4a2), large normal forces (>100 N) occur at the bottom lower edge of the block as it collides onto the floor and is sheared off. In the meantime, the large normal forces also propagate upward into the block, leading to some new cracks. Two broken curves are plotted in Figure 4a2 to indicate the concentration of dominant forces. The corresponding two major cracks can be observed in Figure 4b3, resulting in block and chipping fragments. As shown in Figures 4a2 and 4b2, it is clear that after impact, fragments in the bottom wedged region detach from the initial rock block quickly, on

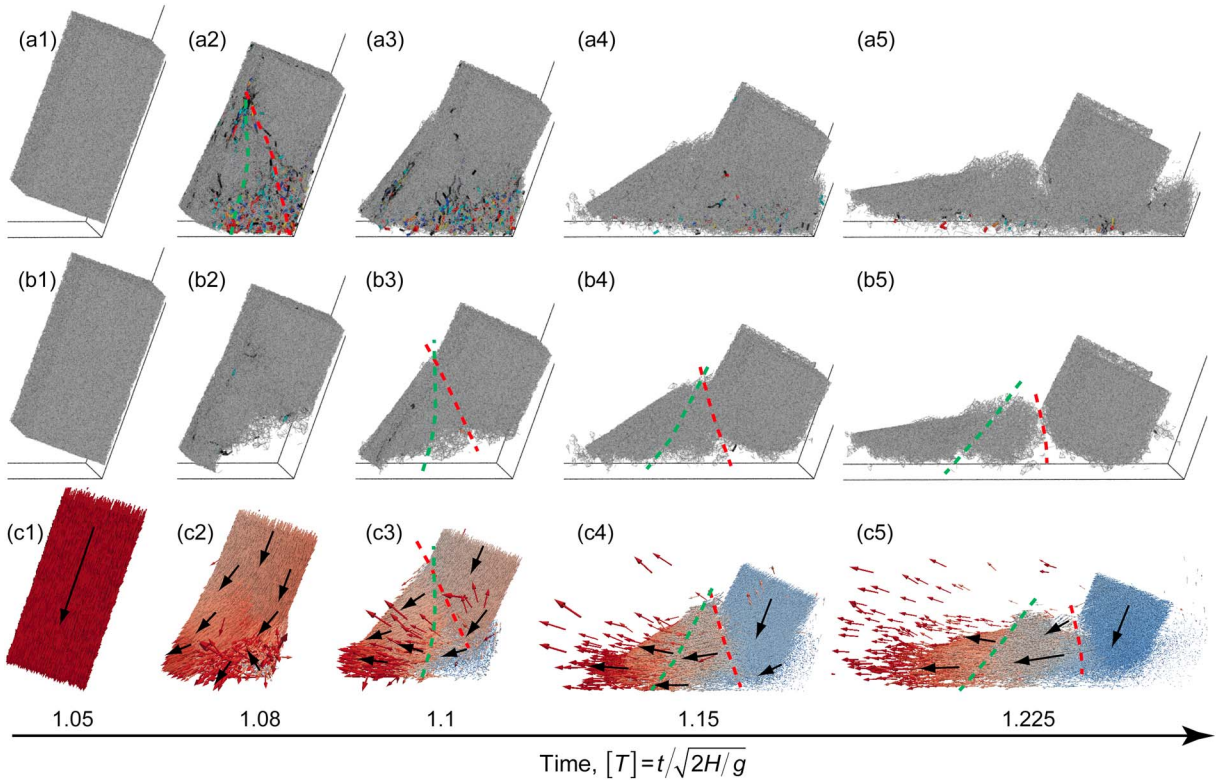

Figure 4. Example of the evolution of (a1–a5) the total force chains; (b1–b5) the bond force chains; and (c1–c5) the granular velocity field during a simulation of $\theta = 70°$. The thickness of the chains is proportional to the force magnitude, and gray if force is smaller than 50 N, cyan, blue, yellow, pink, orange, and red if in the range of [50, 60) N, [60, 70) N, [70, 80) N, [80, 90) N, [90, 100) N, and [100, 200] N, respectively. The green and red broken lines in Figure 4a2 shows the concentration of major forces, while the broken lines in Figures 4b3–4b5 indicate the major cracks developed after impact. In Figures 4c1–4c5, the gradual change of color from red to blue shows the velocity variation from 40 to 0 m/s. Black arrows are plotted to indicate the overall movement trend of different sectors of the granular system.

which the rest upper rock mass is sheared off and move horizontally. Then the subsequent crack openings occur at the bottom and upper middle parts of the rock block (see Figures 4b3–4b5). In addition, Figures 4c1–4c5 present the evolution of particle velocity field of the granular system. After impact, the transmission of the wall force into the agglomerate would decelerate the particles above the point of impact, but other particles, e.g., near the bottom left corner of the agglomerate, would not be affected. This leads to a heterogeneous distribution of particle velocities that may indicate any velocity discontinuity, which would subsequently become a fracture plane (see the broken curves).

To analyze the fragment motion, the evolution of the average vertical (v_v), horizontal (v_h), and lateral (v_l) velocity components of rock fragments (normalized by $\sqrt{2gH}$) was monitored (see Figure 5a). It can be observed that before impact ($[T] < 1.08$), v_v and v_h increase linearly, while v_l remains nil. After impact, v_v decreases sharply from 0.93 to 0.41, while v_h first increases quickly from 0.34 to the peak value (0.46) and then decreases slowly to 0. The time interval for the sudden velocity change is 0.5 ms. In this process, the magnitude of v_l remains negligibly small, indicating that the lateral dispersion of fragmented rock mass is limited by the lateral walls. Conversely, the vertical and horizontal spreading motions are dominant.

Analyses of the energy components of the granular flow are helpful for a comprehensive understanding of the mechanism of rock fragmentation and postfailure fragment movements [*Locat et al*., 2006; *Haug et al*., 2016]. Following *Utili et al*. [2015], the potential energy of the rock mass, E_p, is defined with respect to a reference point:

$$E_p = \sum_{i=1}^{N} m_i g H_i \tag{7}$$

with N being the total number of particles, m_i and H_i being the mass and height of particle i, respectively. Also, E_p represents the total energy of the granular system, E_0, before release. The elastic energy of the rock block

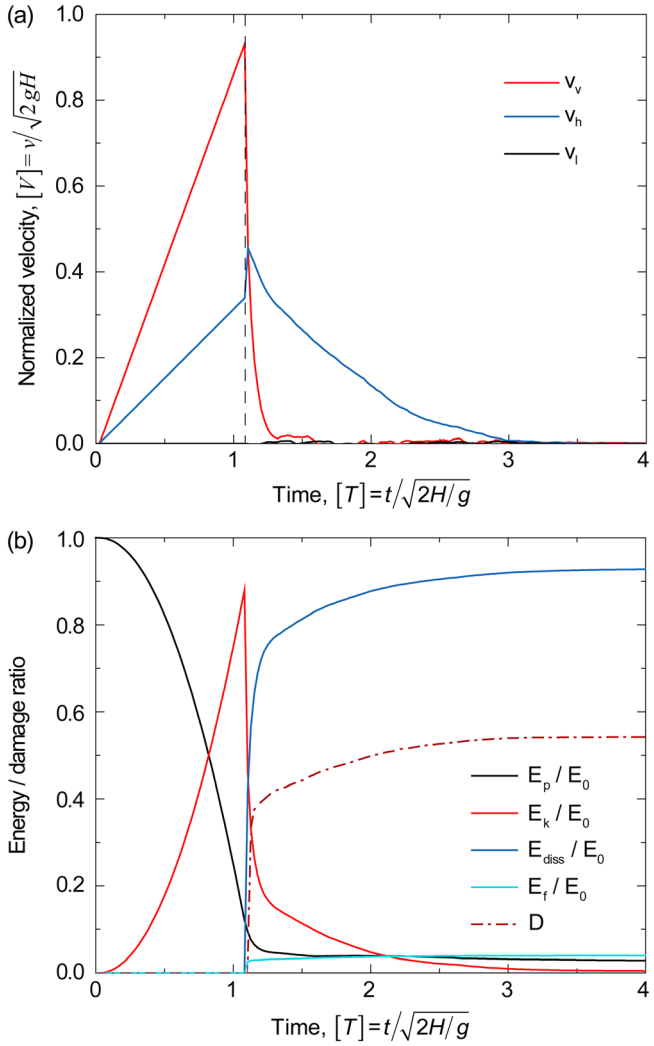

Figure 5. Evolution of (a) normalized average granular velocity components (v_v: vertical velocity component; v_h: horizontal velocity component; and v_l: lateral velocity component) and (b) granular energy and damage ratio (E_{ptotal}: total potential energy; E_k: kinetic energy; E_{diss}: energy dissipation; E_f: fragmentation energy; E_0: initial total energy; D: rock damage ratio) ($\theta = 70°$).

consists of two contributions: the elastic energy stored in each bond, E_b, and at each contact between two particles (energy due to particle elastic deformation near the contact point), E_c. They are calculated as follows:

$$E_b = \frac{F_{bn}^2}{2K_{bn}} + \frac{F_{bs}^2}{2K_{bs}} + \frac{M_b^2}{2K_b} + \frac{M_t^2}{2K_t} \quad (8)$$

$$E_c = \frac{F_n^2}{2K_n} + \frac{F_s^2}{2K_s} \quad (9)$$

The kinetic energy of the rock block is calculated as the summation of the translational and rotational kinetic energy of all the DEM particles, which here mimic the rock grains:

$$E_k = \frac{1}{2}\sum_{i=1}^{N}\left(m_i|v_i|^2 + I_i|\omega_i|^2\right) \quad (10)$$

with $I_i = 0.4m_i r_i^2$ being the momentum of inertia, r_i being the particle radius, and ω_i being the angular velocity. The energy released every time a bond breaks is recorded as the potential energy possessed by the bond at the last time step before breakage occurred. The total fragmentation energy for the rock block, E_f, is calculated as the cumulative energy released by all bond breakages from the beginning of the simulation until the current time. The total cumulative energy dissipated by friction and viscous damping at any given time, E_{diss}, is calculated by subtraction as

$$E_{diss}(t) = E_0 - E_b(t) - E_c(t) - E_k(t) - E_f(t) \quad (11)$$

As shown in Figure 5b, before the block impacts the horizontal plane, no energy is dissipated. After impact, the kinetic energy of the granular system decreases sharply, and more than 90% of the initial total energy (E_0) is dissipated mainly by friction and viscous damping, with fragmentation energy amounting only to 3.95% of the total energy. The numerical results indicate that the energy dissipated by friction and viscous damping during the fragmentation process is large, while the energy consummated to break bonds is small. Low fragmentation energy input in disintegrating the rock mass has been documented by *Locat et al.* [2006] and *Crosta et al.* [2007] on real rock avalanches. In our analyses, the damage ratio (D) [*Thornton et al.*, 1996] has been used to quantify rock fragmentation intensity, which is defined as the ratio of the number of broken bonds after impact to the total number of bonds at the initial static state. According to Figure 5b, it can be observed that the damage ratio increases quickly to around 40% during impact. The subsequent sliding and collision of fragments leads to an additional 10% of bond breakage.

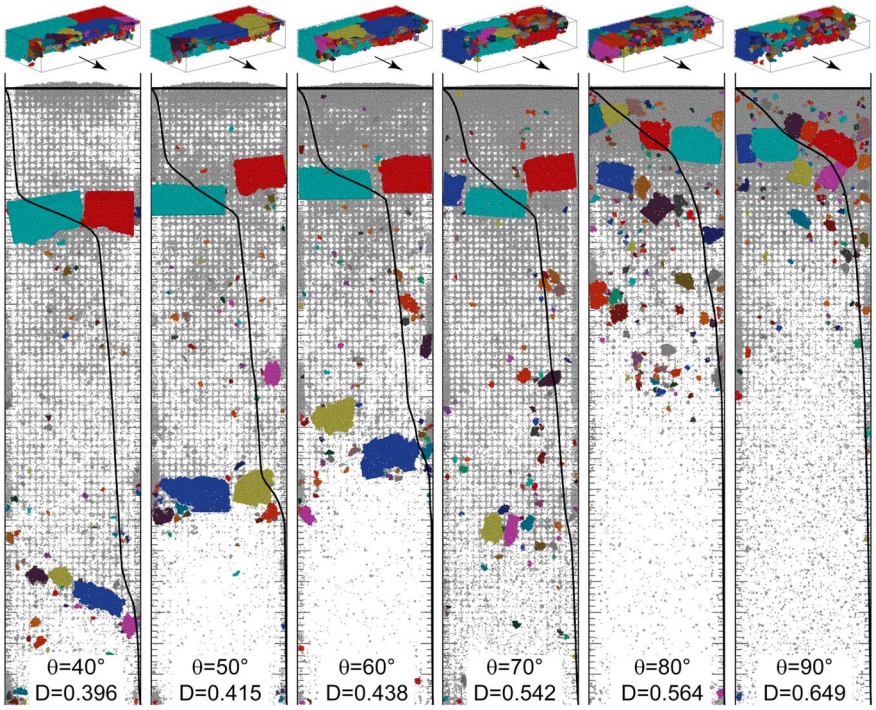

Figure 6. Plan view of the final fragment depositions for simulations with various slope angles. The cumulative mass curve of the granular system along the path is plotted as black curves. Small images at the top show the relative position of the fragments generated at the impact.

3.2. Rock Fragmentation at Various Slope Angles

The slope angle influences the fragmentation and the spreading behavior of rock avalanches, as the smoothness of the transition between the inclined and horizontal portions of the slope affects the deceleration and stress distribution within the rock block significantly [*Strom*, 1999; *Locat et al*., 2006]. According to Figure 6, it can be observed that as the slope angle increases from 40° to 90°, the damage ratio of rock increases progressively from 0.396 to 0.649. In case of gentle slopes ($\theta < 70°$), some relatively large fragments can spread to the front, while for steeper slopes, the rock block is heavily fragmented, producing lots of small fragments in the frontal region. Large fragments (e.g., for the tests of $\theta \geq 50°$) act as a barrier to dispersed particles (grey dots) which consequently are retained close to the slope break. Note that the final fragment depositions qualitatively match the experimental observations in *Bowman et al*. [2012] and *Haug et al*. [2016]. Detailed information about the damage ratio, fragment velocity, and spreading distance of rock blocks tested on slopes with various angles is provided in Table S1 (supporting information). The final fragment size distribution (FSD) exhibits qualitative agreement with the Weibull's function [*Weibull*, 1951; *Brown and Wohletz*, 1995; *Cheong et al*., 2004], as shown in Figure 7. For gentle slopes (e.g., $\theta < 65°$), the mass percentage of fine fragments is very low, and it increases quickly for medium and coarse fragments. However, in case of steep slopes (e.g., $\theta > 65°$), the fragment size distribution tends to be uniform, and the accumulative mass percentage increases gradually with a gentle curvature for the fitting curve. The apparent difference in FSD patterns for these tests can be explained in more detail by considering the loading strain rate dependence of rock fragmentation process, as will be discussed below (see Figure 9).

Generally, the fragment runout decreases with the slope angle increasing, except for the case of $\theta = 70°$ where a sudden increase of runout is apparent (see Figure 6). In this case, the impact-induced fracture stress and relatively high preimpact horizontal velocity can facilitate the motion of small fragments with long runout. The physics of slope-dependent runout is governed by the momentum input to the collision (vertical component) and sliding (horizontal component) processes. Measurements of linear momentum have already proved valuable to characterize the debris flows of granular materials [*Utili et al*., 2015]. For a rock block

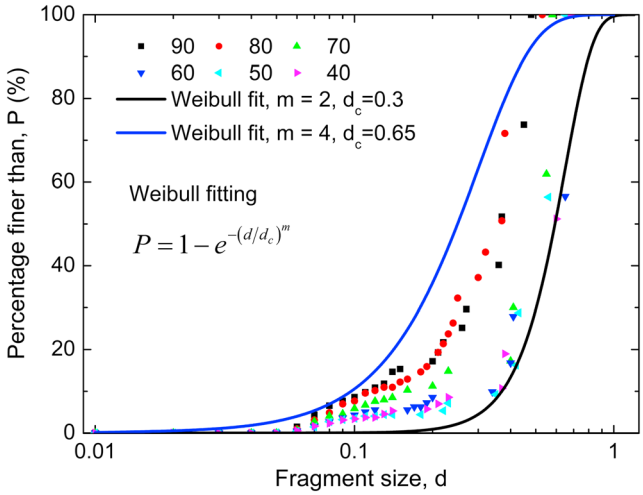

Figure 7. Fragment size distributions of deposits from DEM simulations at different slope angles. Curves are compared to best fitting Weibull's grain size distribution. The nominal fragment size is defined as $d = \sqrt[3]{V_f/V_0}$, with V_f being the volume of the largest fragment and V_0 being the volume of rock block prior to impact.

sliding along a slope of angle θ, before impact, the rock block linear momentum (p) can be decomposed into horizontal (p_h) and vertical (p_v) components as

$$\begin{cases} p_h = p \times \cos(\theta) \\ p_v = p \times \sin(\theta) \end{cases} \quad (0^\circ \leq \theta \leq 90^\circ) \tag{12}$$

According to equation (12), it is clear that at small slope angles, p_v is relatively small, and thus rock fragmentation is not efficient. On the contrary, p_h is large, leading to a long spreading distance. For large slope angles, p_v reaches the maximum value, leading to intensive collisions between the rock block and bottom floor. However, p_h is close to nil, resulting in short runouts. Here it should also be noted that equation (12) only provides the momentum components before impact. The momentum components after impact are different from those calculated from equation (12) due to fragmentation.

Figure 8a illustrates the evolution of vertical and horizontal momentum components for rock blocks tested on various slope inclinations. It can be observed that before impact, the momentum components increase linearly over time. The increasing rate of the horizontal momentum is larger than that of the vertical one, if $\theta < 45°$, while the vertical momentum increases faster if $\theta \geq 45°$. After impact, the vertical momentum component of the granular system decreases sharply to zero within a short time, while the horizontal momentum component increases suddenly to a maximum value and then decreases gradually to zero due to basal friction and fragment interactions. This sudden increase of horizontal momentum is denoted here as momentum boost (see Table 2). Looking at the table, it emerges that the boost of horizontal momentum increases significantly with the slope angle, for the testing cases of $\theta \geq 45°$, becoming infinite at $\theta = 90°$ since in that case the horizontal velocity prior to impact is nil. Conversely, for $\theta < 45°$, no such momentum evolution trend is observed. This trend was postulated by *De Blasio and Crosta* [2015], showing that a critical slope angle exists for the momentum boosting effect of rock fragmentation to take place, and above this critical angle, the horizontal momentum increases more than 5%.

The average impacting forces acting on the rock block in the horizontal (F_h) and vertical (F_v) directions can be expressed as

$$\begin{cases} F_h = \dfrac{(p_{h2} - p_{h1})}{\Delta t} \\ F_v = \dfrac{(p_{v2} - p_{v1})}{\Delta t} \end{cases} \tag{13}$$

where p_{h1}, p_{v1} are the horizontal and vertical momentum components of the rock block before collision, and p_{h2}, p_{v2} are momentum components after the collision. Δt is the collision time (0.5 ms, as defined

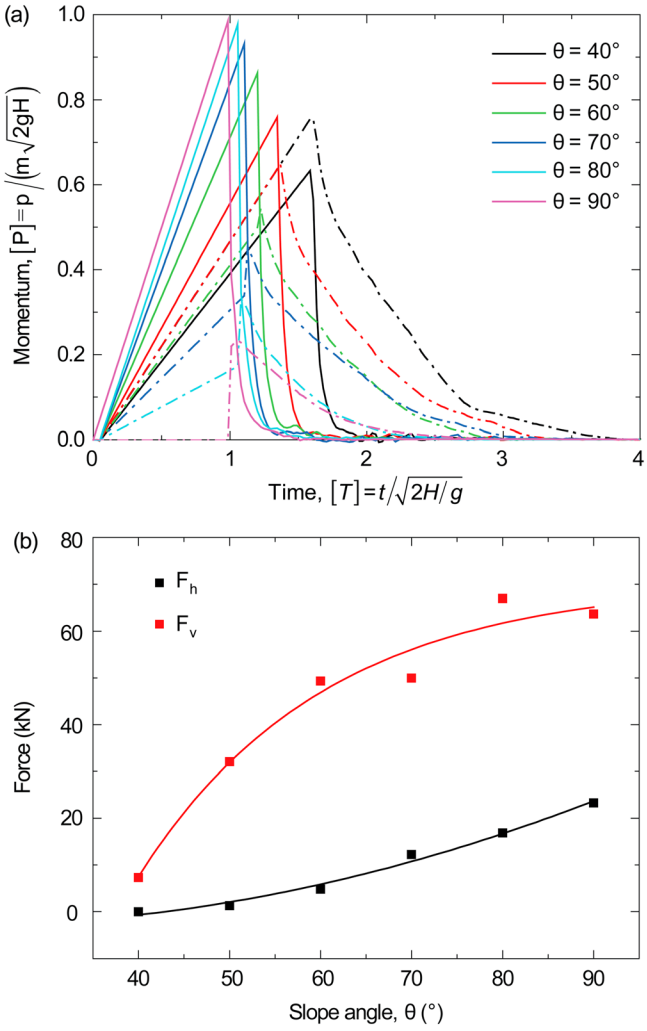

Figure 8. Analysis of granular momentum for tests on various slopes, (a) evolution of the vertical (solid lines) and horizontal (dash-dotted lines) momentum components of the granular system. The momentum is normalized as $[P] = p/(m\sqrt{2gh})$. (b) Average impacting forces.

before). In the current analyses, the positive direction of the horizontal force is set as the direction perpendicular to the slope break and along the granular spreading path, while the positive direction of the vertical force is set as vertically upward.

Theoretically, the vertical impacting force would contribute to the rock fragmentation as it is perpendicular to the impact plane, while the horizontal impacting force would influence the fragment spreading along the bottom floor. Figure 8b illustrates the average impacting forces acting on the granular assembly in the horizontal and vertical directions. The numerical results indicate that the rock fragmentation can be very intense on steep slopes and more frontal impacts (e.g., with increased direct impacting area), which is also indicated by the increased damage ratio (D) (see Figure 6). As for the horizontal impacting force, it could consist of basal friction, contact force between fragments, and the interaction with the inclined slope. It acts to eject the detached rock fragments forward along the bottom floor. According to Figure 8b, it is clear that on a gentle slope ($\theta = 40°$), the horizontal impacting force can be negative, which implies that the basal friction is dominant to decelerate the granular motion.

Since the vertical component of impact velocity is directly related to the strain rate of rock fragmentation, it is evident that the impacting process is loading rate dependent, such that the rock fragmentation intensity increases with the impact loading strain rate. In this study, the impact loading strain rate is defined as v_v/l, with l being the sample length in the sliding direction. Depending on slope inclination, the loading rate ranges from 275 s^{-1} to 428 s^{-1}, while the corresponding damage ratio (D) increases from 0.396 to 0.649. As discussed before, the peak strength and deformation of rock can increase quickly at high loading rates (see also Figure S1 in the supporting information). The dynamic shear strength of coal rock in this study ranges from 27 MPa to 41 MPa, while in comparison the shear strength under quasi-static conditions is only 9.82 MPa (see Figure 1). As a general explanation, it can be said that a large amount of energy is needed for rock fragmentation on very steep slopes where high strain rates arise at impact. This can lead to accumulation of large amounts of elastic energy. After failure, this elastic energy leads to very intense rock fragmentation and abrupt ejections of fine fragments.

To characterize the fragment size, the nominal fragment size is defined as $d = \sqrt[3]{V_f/V_0}$, with V_f being the volume of the largest fragment, and V_0 being the volume of rock block prior to impact. In addition, the impact-induced fracture stress can be calculated as $\sigma = F_v/(A/\sin(\theta))$, with A being the area of the block front face. The dependence of the nominal fragment size and fracture stress on the impact loading strain rate is

Table 2. Boost of Horizontal Momentum at Impact (Δp_h Is the Increase of Momentum at Impact, and p_{h0} Is the Momentum Prior to Impact)[a]

Slope Angle (deg)	50	60	70	80	90
Δp_h (kg m/s)	0.63	2.40	6.11	8.437	11.64
$\Delta p_h/p_{h0}$	1.9%	9.1%	34.1%	92.5%	∞
Analytical solutions	7.7%	17.9%	45.2%	129.6%	∞

[a]The analytical solution is given in *De Blasio and Crosta* [2015] for a rock fragmentation at an impact velocity of 20 m/s.

illustrated in Figure 9. It is clear that the nominal fragment size decreases, while the fracture stress increases with the impact loading strain rate. The increase of fracture stress is also associated with a sharp increase of damage ratio (D). The obtained numerical results exhibit the same trends as those reported in *Grady and Kipp* [1985] (see the inset plots in Figure 9). At low loading rates, the induced fracture stress is low (see Figure 9b), and relatively few fractures occur within the rock block. Thus, the resultant fragment size is relatively large (see Figure 9a). On the contrary, at high loading rates, the input energy and impact-induced fracture stress are high (see Figure 9b). Thus, a large amount of fractures can be generated within the rock block. Consequently, fractures can nucleate and grow to completion quickly, leading to relatively small fragments (see Figure 9a).

Figure 10 shows how the fragment number (N) is related to damage ratio (D) and impact loading strain rate. In the tests, the fragment number is determined by counting the agglomerate pieces consisting of at least 10 particles. It emerges that the fragment number increases with the damage ratio (see Figure 10a), indicating that a rock block with high damage ratio produces a large amount of fragments after the impact. This feature is in agreement with previous experimental observations on ductile aluminum rings by *Grady and Kipp* [1985], since the breakage of bonds contribute to the nucleation and growth of fractures leading to the production of many fragments with relatively small sizes. Figure 10b illustrates the dependence of fragment number (N) on impact loading strain rate ($\dot{\varepsilon}$). It can be observed that N increases with the impact loading rate slowly for $\dot{\varepsilon} \leq 375\ s^{-1}$, whereas it increases sharply at higher loading rates. The numerical results show a generally similar increasing trend as the experimental data by *Grady and Kipp* [1985], even though the testing method and material are different. However, the difference on the fragment number and fitting curve relationships between these two types of tests lies in the material property and impact loading strain rate. It is evident that the brittle coal rock in this study can be easily fragmented at low loading rate (i.e., $<10^3\ s^{-1}$), whereas the ductile aluminum in *Grady and Kipp* [1985] can resist more effectively the impact induced breakage at higher loading rates (i.e., $>10^3\ s^{-1}$).

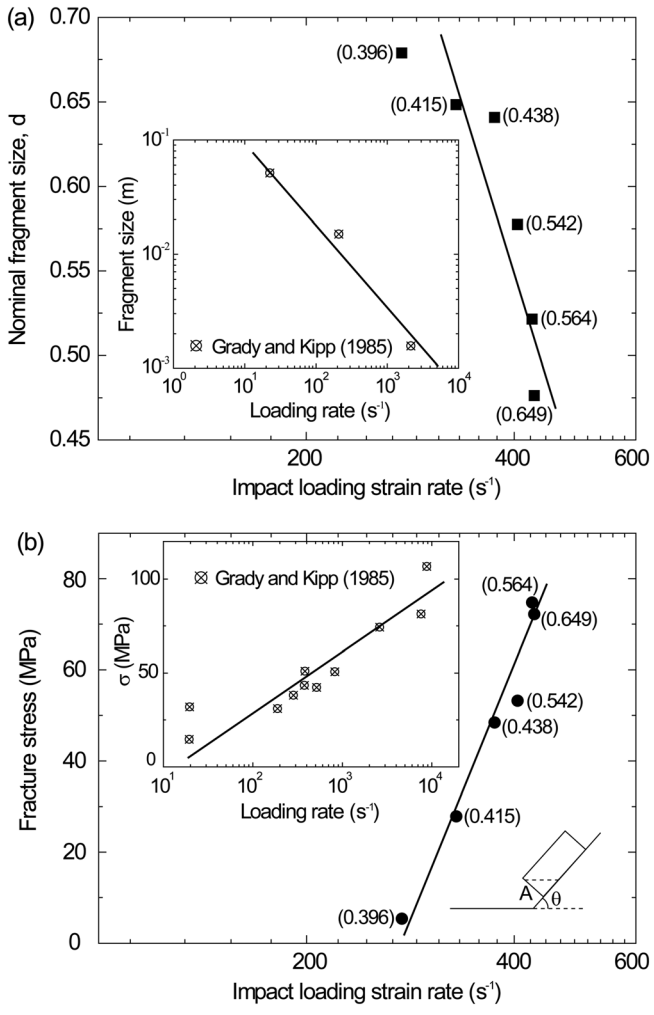

Figure 9. Dependence of (a) nominal fragment size and (b) fracture stress on the impact loading strain rate. The rock damage ratio (D) for the corresponding tests is plotted near the data points. The inset plots show the experimental data reported in *Grady and Kipp* (1985), and the sketch represents how the fracture stress is computed according the equation $\sigma = F_v/(A/\sin\theta)$.

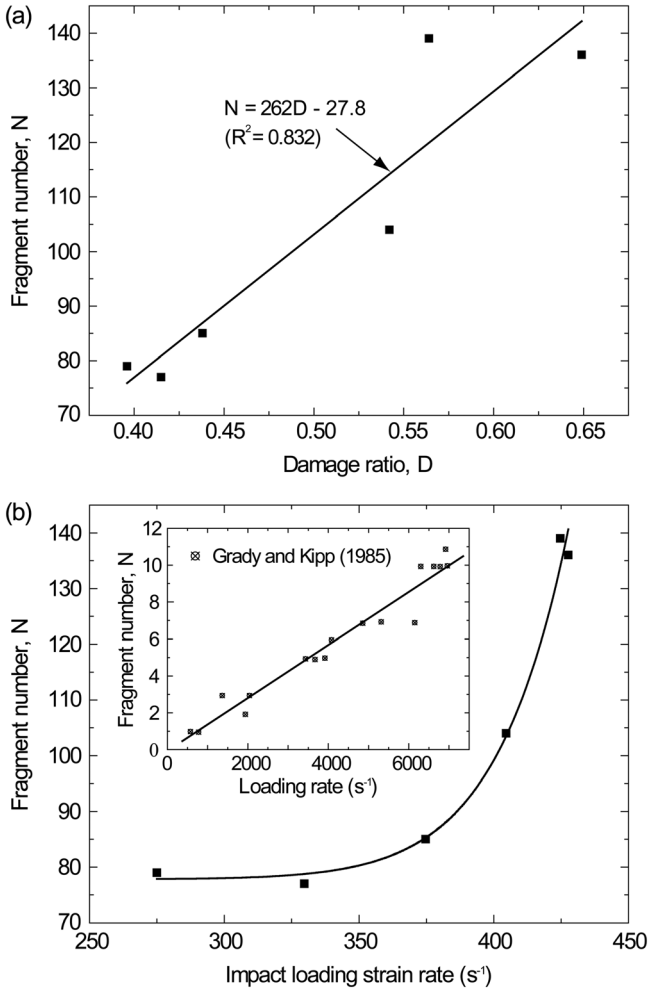

Figure 10. Fragment number (*N*) versus (a) the damage ratio (*D*) and (b) impact loading strain rate. The inset plot in Figure 10b shows the experimental data on ductile aluminum rings reported in *Grady and Kipp* [1985].

4. Discussion

The simulations presented in this study were aimed at reproducing the experiments of rock block fragmentation at the slope break [*Bowman et al.*, 2012; *Haug et al.*, 2016]. Although such experiments mimic the geometry of a real rock avalanche at a small scale, when applying such works to field studies the problem arises as to what extent small-scale experiments and related simulations are representative of field observations.

A first issue is the confinement of the traveling mass. In order to mimic the experimental configuration used in *Bowman et al.* [2012], in the current study the movement of fragments was confined within a narrow channel. However, due to the constrained lateral dispersion of fragments after impact, this approach inevitably leads to intensive interactions between fragments and the confining walls at the lateral boundary. Consequently, fragments running to the boundary bounce back into the channel, influencing the motion of fragments and fragmentation itself [*Erismann and Abele*, 2001]. In fact, in the field the lateral dispersion of the granular trajectories has been widely observed, when falling rock blocks collide onto the ground [*Crosta et al.*, 2017; *Haug et al.*, 2016]. This feature of rock slides, falls, and avalanches can be important for assessing hazard and providing guidelines to design of defense systems. To better investigate this influence, we have extended our simulations by running a series of simulations with unconfined lateral boundary condition. Figure 11 shows the testing condition of $\theta = 90°$ for the unconfined collapse. For comparison purposes, the locations of the channel boundary of the confined testing condition calculated earlier are plotted as two parallel bold blue lines. Our simulations show that the lateral dispersion of fragments occurs immediately after the impact, and that the lateral spreading area increases with time. The final distribution profile of the boundary solids is shown as a red dashed curve in Figure 11e, with a bulged bowl shape. Figure 11f shows the final deposition of rock fragments obtained from tests with confined boundaries (see Figure 6). The comparison clearly shows that in contrast with the confined testing condition where clasts accumulate near the slope toe area, unconfined setting allows the large fragments to spread also laterally in a subcircular pattern.

Based on Figure 11e, we can define the lateral dispersion ratio of rock fragments as W/L_s, with W being the maximum lateral dispersion distance and L_s the fragment runout distance. The relationship between the lateral dispersion ratio of rock fragment and slope angle is plotted in Figure 12a. The values of W/L_s for tests with confined boundaries are also plotted for the sake of comparison, with W taken as a fixed value equal to the channel width. According to Figure 12a, the W/L_s ratio increases with slope inclination, indicating that the lateral dispersion of rock fragments becomes increasingly intensive for rock

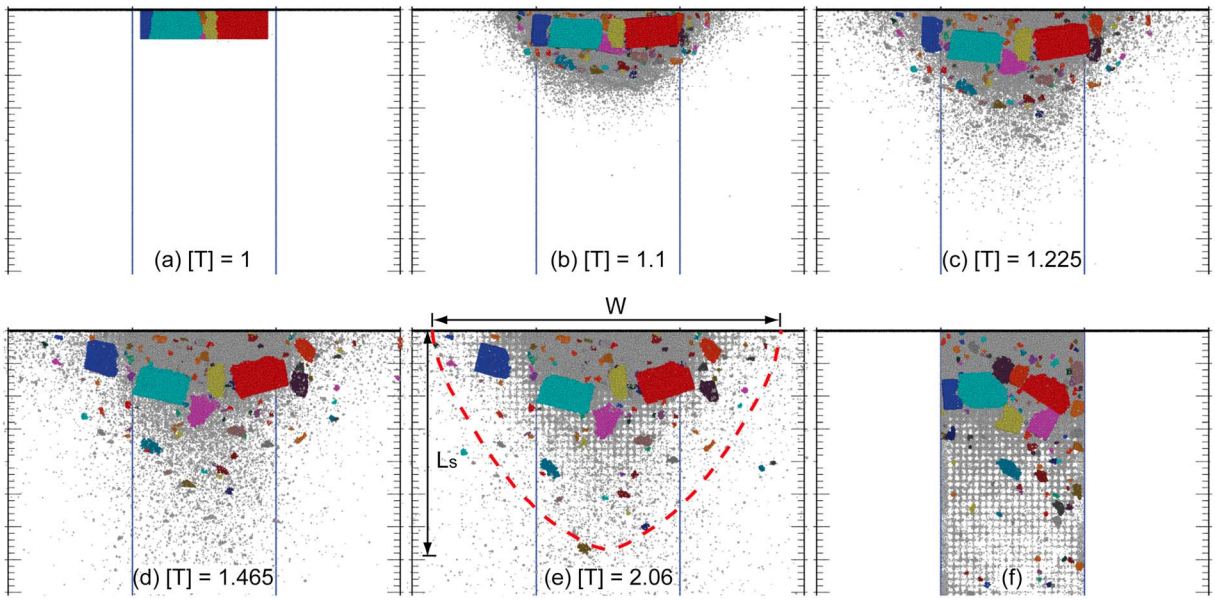

Figure 11. (a–f) Lateral dispersion of fragments for $\theta = 90°$. The two parallel blue lines represent the locations of the channel boundary for the confined testing condition. In Figure 11e, the dashed curve represents the approximate fragment deposition profile, with *W* being the lateral dispersion distance, *Ls* being the maximum runout distance. Figure 11f is the final fragment deposit as in Figure 6 for laterally confined conditions $\left([T] = t/\sqrt{2H/g}\right)$.

blocks tested on steep slopes. Comparison between the unconfined and confined boundary tests illustrates that W/L_s remains the same for both tests if $\theta \leq 60°$, while it becomes increasingly larger in the unconfined boundary tests if $\theta > 60°$. This phenomenon indicates that the effect of fragment lateral dispersion is significant only in steep slopes. The numerical results for the unconfined and confined tests can be fitted with good accuracy by an exponential and a linear relationship, respectively. Looking at Figure 12a, it is worth to observe that the W/L_s ratio is quite low (≈ 0.2) for gentle slopes ($\leq 40°$). This agrees with the observations reported by *Haug et al*. [2016] of an elongated propagation and deposition area taking place in their experiments on a 45° inclined slope. Instead in Figure S3 (supporting information), the results of a DEM simulation, based on *Haug et al*. [2016] geometrical constraints but under augmented gravity, are plotted. The distribution of the material qualitatively agrees with their experimental observations.

The DEM results are analyzed with regard to mobility in Figure 12b, where the *H*/*L* ratio (i.e., apparent friction coefficient, *H*: the drop height; *L*: the spreading length) is plotted with respect to the slope angle. In the figure, the results for the simulation of a DEM model made of loose grains, with a configuration similar to the one adopted by *Crosta et al*. [2017], are also presented. The data show an increase of *H*/*L* with slope inclination, suggesting that the granular motion encounters high resistance on steep slopes with strong energy absorption at impact. The data qualitatively follow the real rock avalanche/fall observations and are well fitted by the relationship proposed by *Crosta et al*. [2017]. Best fitting of the simulation results requires a relatively large transverse coefficient of restitution, ε, as defined by *Crosta et al*. [2017], i.e., ratio of the horizontal velocity component acquired upon impact to the vertical velocity before impact, with respect to analyses performed for loose materials. The definition of ε accounts for the momentum boost effect during impact, as discussed before. This is also expressed by preimpact and postimpact velocities reported in Table S1 (supporting information), and it could be associated with the stiffness of the falling block with respect to the loose case study. The confined and unconfined DEM tests can lead to very similar results, except for cases with very steep slopes. For these tests (e.g., $\theta > 80°$), the lateral dispersion effect with high friction resistance is evident for the unconfined boundary condition, and thus the fragment runout is relatively short. For the loose DEM simulations, the spherical particle shape and elastic interactions significantly decrease both the basal friction and energy absorption at impact. Thus, the granular materials show higher mobility (i.e., low H/L ratio) than fragments resulted from rockfall impact tests.

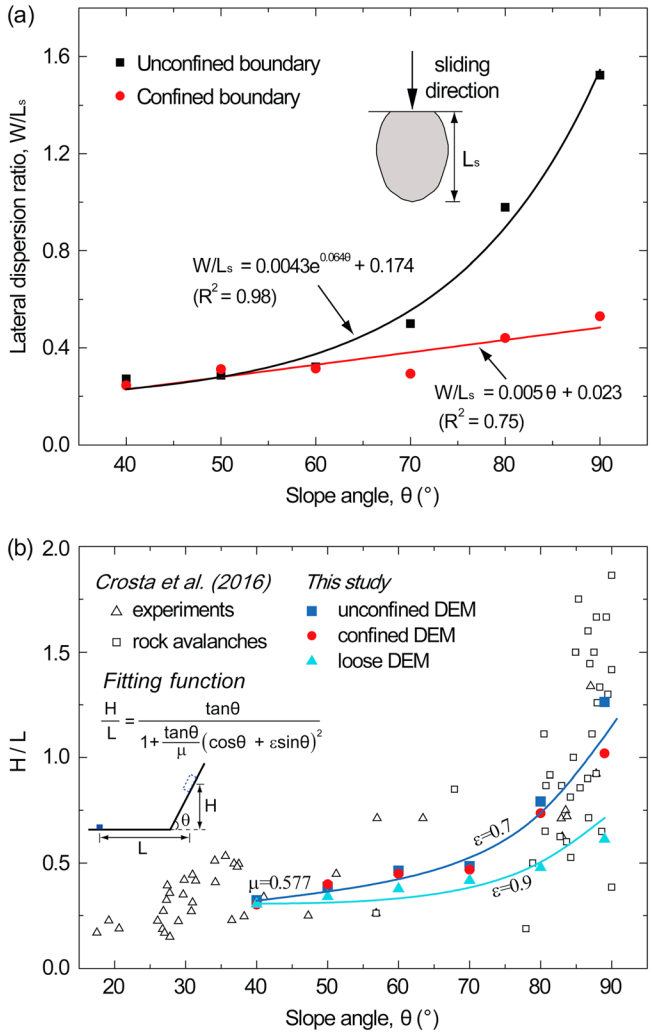

Figure 12. Dependence of (a) dispersion ratio (i.e., channel or deposit width to runout distance, L_s) and (b) the apparent friction coefficient (H/L) on the slope angle. The ratios of both the laterally confined and unconfined tests are plotted. In Figure 12b the DEM results for H/L are compared to experimental and real rock avalanche data and to the equation proposed by *Crosta et al.* [2017]. The best fitting function accounts for the model geometry of smooth slope and rough floor. $\mu = 0.577$ is the friction coefficient of the basal floor.

The relevance of impact fragmentation at controlling the final fragment size distribution and the runout of deposits of highly energetic mass movements is an interesting research subject that can be tackled by DEM simulations. The impact-induced fragmentation in the numerical DEM simulations performed in this study occurs within a very short time period, during which a high percentage of interparticle bonds break and some energy is released (i.e., loss of energy). This sudden and only collision, which in our numerical simulations results from the assumption of a simple bilinear slope path, is undoubtedly an approximation of reality. Although many real rock avalanche paths look like a bilinear geometry [*Crosta et al.*, 2017], as the one considered here, one should consider the unevenness of large-scale topography (e.g., large obstacles, impact against the opposite valley flank), which often causes multiple impacts in real events. In addition, irregularities at small scale such as small indentation and slope roughness may play an important role in fragmentation as well [*De Blasio and Crosta*, 2014]. Finally, a certain degree of fragmentation is probably associated with initial rock mass fracturing at the release and exit of the source area.

Notwithstanding the simplification inherent in a bilinear slope path, it can be expected that this geometry is capable of capturing the first major impact, which will be associated with the highest rock damage and energy dissipation. Thus, it can be helpful to analyze the potential relationship between the instantaneous bond breakage ratio (*BR*) and energy dissipated for various testing conditions. Note that the definition of *BR* is different from the previously defined damage ratio (*D*), because only bond breakages occurring during the first impact are considered, while the bond breakages by subsequent fragment sliding and collisions are ignored. In the current analyses, the instantaneous dissipated energy, computed as the difference between the total cumulative dissipated energy before (t_1) and after (t_2) the sudden impact, is normalized by the initial potential energy of the rock block and denoted as E_d^*.

$$E_d^* = [E_{\text{diss}}(t_2) - E_{\text{diss}}(t_1)]/E_0 \tag{14}$$

In Figure 13, the relationship between *BR* and E_d^* for the confined and unconfined testing cases is presented. It is clear that the energy dissipated at impact increases with *BR*, for these two types of tests, following exponential relationships. On gentle slopes (e.g., $\theta = 40°$), *BR* can be less than 0.25, and the corresponding energy dissipation is around 0.6. However, on steep slopes (e.g., $\theta = 90°$), *BR* becomes larger than 0.6, and E_d^* is

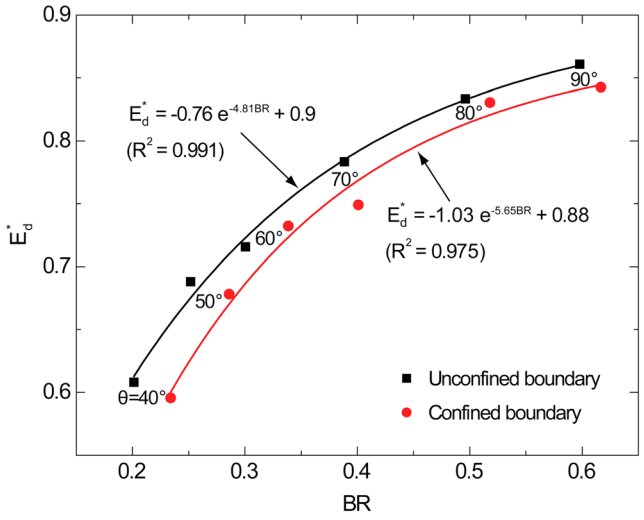

Figure 13. Plot of the energy dissipation versus the instantaneous bond breakage ratio (*BR*) (the testing slope angle is labeled close to the data points).

around 0.85. The numerical results indicate that the rock fragmentation intensity is associated with the input energy and increases quickly with the slope angle. The comparison between laterally confined and unconfined tests also shows that the energy dissipated by rock fragmentation tested without lateral confinement is slightly larger than the one tested with confinement, indicating that lateral confinement can constrain energy dissipation in rock fragmentation.

Finally, it is worth to mention the role that load intensity and strain rate have on the fragmentation process. Numerical simulations put in evidence the increase in fragmentation (i.e., number of fragments, decrease in fragment size) at increasing strain rate beyond a specific threshold value. The same holds true, according to the numerical results, for load intensity, with more intense fragmentation observed in case of high loads. Both these findings agree with observations in the literature [*Grady and Kipp*, 1985] and could explain why in nature we can observe very different degrees of fragmentation for processes we classify solely as rockfalls or rock avalanches. In fact, the same classes of phenomena are characterized by very different geometrical features of both the released mass and the slope profile.

5. Conclusions

This paper presents the results of numerical investigations by 3-D discrete element method simulations of the fragmentation of prismatic rock blocks when reaching a sharp break at the base of a simple slope. The use of parallel bonds to mimic cementation between rock grains has enabled the measurements of internal forces, energy, and damage intensity of rock blocks during impact, which are not currently achievable from experimentation. The obtained results reveal the characteristics of dynamic rock fragmentation and the mechanism governing the postfailure fragment motion.

The sudden collision of rock blocks onto the bottom floor leads to instantaneous increase of normal forces at the bottom lower edge of the block, producing several large blocks and many small fragments. Then, the impacting force wave propagates upward into the rock mass, leading to some new cracks and subsequent damages of the rock block. For rock slide on a slope of 70° inclination, around 40% of interparticle bonds break immediately at impact, and then less than 10% of bonds breaks due to the subsequent sliding and collision of fragments. This process causes more than 90% of energy dissipation by friction and plastic deformation of rock grains, while only a small portion ($<$5%) of energy by bond breakage.

To mimic various natural slope topographies, simulations for a range of slope angles were performed. Tests on gentle slopes normally lead to long spreading distance, whereas tests on steep slopes exhibit high impact strain rates and efficient fragmentation. Apparent granular momentum boosting can be observed for tests with slope angles larger than 50°, and the horizontal momentum can increase by more than 5% in various testing conditions. This means that fragmentation is capable of enhancing velocity and mobility of the fragments, thus converting vertical into horizontal momentum. There is obviously no violation of momentum conservation, because the extra horizontal momentum is taken up by the terrain at the slope break [*Crosta et al*., 2017]. For these tests, the fracture stress, fragment number, damage ratio, and the overall apparent friction coefficient of rock fragment runout all increase, while the nominal fragment size decreases with the impact loading strain rate. The fragment size distributions resulting from the DEM simulations approximate well a Weibull's distribution.

Acknowledgments

The data are available upon request from the authors. This research was supported by the National Natural Science Foundation of China (grant 41602289), EU H2020 RISE programme "Geo-ramp" (grant 645665), the opening fund of State Key Laboratory of Geohazard Prevention and Geoenvironment Protection (Chengdu University of Technology) (grant SKLGP2016K022), and the Youth Science and Technology Fund of Sichuan Province (grant 2016JQ0011). The constructive comments from two anonymous reviewers helped at improving the manuscript.

References

Agliardi, F., and G. B. Crosta (2003), High resolution three-dimensional numerical modelling of rockfalls, *Int. J. Rock Mech. Min. Sci.*, *40*(4), 455–471, doi:10.1016/S1365-1609(03)00021-2.

Boon, C. W., G. T. Houlsby, and S. Utili (2014), New insights in the 1963 Vajont slide using 2D and 3D distinct element method analyses, *Geotechnique*, *64*(10), 800–816.

Boon, C. W., G. T. Houlsby, and S. Utili (2015), A new rock slicing method based on linear programming, *Comput. Geotech.*, *65*, 12–29, doi:10.1016/j.compgeo.2014.11.007.

Bowman, E. T., W. A. Take, K. L. Rait, and C. Hann (2012), Physical models of rock avalanche spreading behaviour with dynamic fragmentation, *Can. Geotech. J.*, *49*(4), 460–476, doi:10.1139/t2012-007.

Brown, W. K., and K. H. Wohletz (1995), Derivation of the Weibull distribution based on physical principles and its connection to the Rosin–Rammler and lognormal distributions, *J. Appl. Phys.*, *78*(4), 2758–2763, doi:10.1063/1.360073.

Calvetti, F., G. Crosta, and M. Tatarella (2000), Numerical simulation of dry granular flows: From the reproduction of small-scale experiments to the prediction of rock avalanches, *Riv. Ital. Geotecnica*, *21*(2), 21–38.

Cheong, Y. S., G. K. Reynolds, A. D. Salman, and M. J. Hounslow (2004), Modelling fragment size distribution using two-parameter Weibull equation, *Int. J. Miner. Process.*, *74*(Supplement), S227–S237, doi:10.1016/j.minpro.2004.07.012.

Collins, G. S., and H. J. Melosh (2003), Acoustic fluidization and the extraordinary mobility of sturzstroms, *J. Geophys. Res.*, *108*(B10), 2473, doi:10.1029/2003JB002465.

Corominas, J. (1996), The angle of reach as a mobility index for small and large landslides, *Can. Geotech. J.*, *33*(2), 260–271, doi:10.1139/t96-005.

Crosta, G. B., S. Imposimato, D. Roddeman, S. Chiesa, and F. Moia (2005), Small fast-moving flow-like landslides in volcanic deposits: The 2001 Las Colinas Landslide (El Salvador), *Eng. Geol.*, *79*(3–4), 185–214, doi:10.1016/j.enggeo.2005.01.014.

Crosta, G. B., P. Frattini, and N. Fusi (2007), Fragmentation in the Val Pola rock avalanche, Italian Alps, *J. Geophys. Res.*, *112*, F01006, doi:10.1029/2005JF000455.

Crosta, G. B., F. V. De Blasio, M. De Caro, G. Volpi, S. Imposimato, and D. Roddeman (2017), Modes of propagation and deposition of granular flows onto an erodible substrate: Experimental, analytical, and numerical study, *Landslides*, *14*(1), 47–68, doi:10.1007/s10346-016-0697-3.

Cundall, P. A., and O. D. L. Strack (1979), A discrete numerical model for granular assemblies, *Geotechnique*, *29*(1), 47–65, doi:10.1680/geot.1979.29.1.47.

Davies, T. R., and M. J. McSaveney (1999), Runout of dry granular avalanches, *Can. Geotech. J.*, *36*(2), 313–320, doi:10.1139/t98-108.

De Blasio, F., and G. B. Crosta (2015), Fragmentation and boosting of rock falls and rock avalanches, *Geophys. Res. Lett.*, *42*, 8463–8470, doi:10.1002/2015GL064723.

De Blasio, F., and G. Crosta (2014), Simple physical model for the fragmentation of rock avalanches, *Acta Mech.*, *225*(1), 243–252, doi:10.1007/s00707-013-0942-y.

De Blasio, F. V. (2009), Rheology of a wet, fragmenting granular flow and the riddle of the anomalous friction of large rock avalanches, *Granul. Matter*, *11*(3), 179–184, doi:10.1007/s10035-009-0134-6.

De Blasio, F. V., and A. Elverhøi (2008), A model for frictional melt production beneath large rock avalanches, *J. Geophys. Res.*, *113*, F02014, doi:10.1029/2007JF000867.

De Blasio, V. F. (2007), Production of frictional heat and hot vapour in a model of self-lubricating landslides, *Rock Mech. Rock. Eng.*, *41*(1), 219–226, doi:10.1007/s00603-007-0153-8.

Dunning, S. A. (2006), The grain-size distribution of rock-avalanche deposits in valley-confined settings, *Ital. J. Eng. Geol. Environ.*(Special Issue 1 (NATO Advanced Research Workshop, Security of Natural and Artificial Rockslide Dams, Kyrgyzstan, 8-13 June 2004)), *1*, 117–121.

Erismann, T. H., and G. Abele (2001), *Dynamics of Rockslides and Rockfalls*, 316 pp., Springer, Berlin.

Fuenkajorn, K., and N. Kenkhunthod (2010), Influence of loading rate on deformability and compressive strength of three Thai sandstones, *Geotech. Geol. Eng.*, *28*(5), 707–715, doi:10.1007/s10706-010-9331-7.

Goguel, J. (1978), Scale-dependent rockslide mechanisms, with emphasis on the role of pore fluid vaporization, in *Rockslides and Avalanches*, edited by B. Voight, pp. 693–706, Elsevier, Amsterdam.

Grady, D. E. (1981), Fragmentation of solids under impulsive stress loading, *J. Geophys. Res.*, *86*(B2), 1047–1054, doi:10.1029/JB086ib02p01047.

Grady, D. E., and M. E. Kipp (1985), Mechanisms of dynamic fragmentation: Factors governing fragment size, *Mech. Mater.*, *4*(3), 311–320, doi:10.1016/0167-6636(85)90028-6.

Habib, P. (1975), Production of gaseous pore pressure during rock slides, *Rock Mech.*, *7*(4), 193–197, doi:10.1007/bf01246865.

Haug, Ø. T., M. Rosenau, K. Leever, and O. Oncken (2016), On the energy budgets of fragmenting rockfalls and rockslides: Insights from experiments, *J. Geophys. Res. Earth*, *121*, 1310–1327, doi:10.1002/2014JF003406.

Heim, A. (1882), Der Bergsturz von Elm, *Z. Dtsch. Geol. Ges.*, *34*, 74–115.

Hermanns, R. L., et al. (2013), Systematic mapping of large unstable rock slopes in Norway, in *Landslide Science and Practice: Volume 1: Landslide Inventory and Susceptibility and Hazard Zoning*, edited by C. Margottini, P. Canuti, and K. Sassa, pp. 29–34, Springer, Berlin, doi:10.1007/978-3-642-31325-7_3.

Hungr, O., and S. G. Evans (2004), Entrainment of debris in rock avalanches: An analysis of a long run-out mechanism, *Geol. Soc. Am. Bull.*, *116*(9), 1240–1252.

Hutter, K., T. Koch, C. Pluss, and S. B. Savage (1995), The dynamics of avalanches of granular-materials from initiation to runout. 2. Experiments, *Acta Mech.*, *109*(1-4), 127–165, doi:10.1007/Bf01176820.

Imre, B., J. Laue, and S. Springman (2010), Fractal fragmentation of rocks within sturzstroms: Insight derived from physical experiments within the ETH geotechnical drum centrifuge, *Granul. Matter*, *12*(3), 267–285, doi:10.1007/s10035-009-0163-1.

Itasca (2003), *PFC3D: Theory and Background*, 97 pp., Itasca Consulting Group, Inc., Minneapolis, Minn.

Iverson, R. M., M. E. Reid, M. Logan, R. G. LaHusen, J. W. Godt, and J. P. Griswold (2011), Positive feedback and momentum growth during debris-flow entrainment of wet bed sediment, *Nat. Geosci.*, *4*(2), 116–121.

Legros, F. (2002), The mobility of long-runout landslides, *Eng. Geol.*, *63*(3–4), 301–331, doi:10.1016/S0013-7952(01)00090-4.

Li, Y., and C. Xia (2000), Time-dependent tests on intact rocks in uniaxial compression, *Int. J. Rock Mech. Min. Sci.*, *37*(3), 467–475, doi:10.1016/S1365-1609(99)00073-8.

Linares-Guerrero, E., C. Goujon, and R. Zenit (2007), Increased mobility of bidisperse granular avalanches, *J. Fluid Mech.*, *593*, 475–504.

Liu, X., F. Dai, R. Zhang, and J. Liu (2015), Static and dynamic uniaxial compression tests on coal rock considering the bedding directivity, *Environ. Earth Sci.*, *73*(10), 5933–5949, doi:10.1007/s12665-015-4106-3.

Locat, P., R. Couture, S. Leroueil, J. Locat, and M. Jaboyedoff (2006), Fragmentation energy in rock avalanches, *Can. Geotech. J.*, *43*(8), 830–851, doi:10.1139/t06-045.

McDowell, G. R., and M. D. Bolton (1998), On the micro-mechanics of crushable aggregates, *Geotechnique*, *48*(5), 667–679.

Murugaratnam, K., S. Utili, and N. Petrinic (2015), A combined DEM-FEM numerical method for Shot Peening parameter optimisation, *Adv. Eng. Softw.*, *79*, 13–26.

Okubo, S., K. Fukui, and Q. Qingxin (2006), Uniaxial compression and tension tests of anthracite and loading rate dependence of peak strength, *Int. J. Coal Geol.*, *68*(3–4), 196–204, doi:10.1016/j.coal.2006.02.004.

Phillips, J. C., A. J. Hogg, R. R. Kerswell, and N. H. Thomas (2006), Enhanced mobility of granular mixtures of fine and coarse particles, *Earth Planet. Sci. Lett.*, *246*(3–4), 466–480.

Potyondy, D. O., and P. A. Cundall (2004), A bonded-particle model for rock, *Int. J. Rock Mech. Min. Sci.*, *41*(8), 1329–1364, doi:10.1016/j.ijrmms.2004.09.011.

Rait, K. L., E. T. Bowman, and C. Lambert (2012), Dynamic fragmentation of rock clasts under normal compression in sturzstrom, *Géotechnique Lett.*, *2*(3), 167–172.

Ruiz-Carulla, R., J. Corominas, and O. Mavrouli (2016), A fractal fragmentation model for rockfalls, *Landslides*, (in press), 1–15, doi:10.1007/s10346-016-0773-8.

Scheidegger, A. E. (1973), On the prediction of the reach and velocity of catastrophic landslides, *Rock Mech.*, *5*(4), 231–236, doi:10.1007/bf01301796.

Shimizu, H., T. Koyama, T. Ishida, M. Chijimatsu, T. Fujita, and S. Nakama (2010), Distinct element analysis for Class II behavior of rocks under uniaxial compression, *Int. J. Rock Mech. Min. Sci.*, *47*(2), 323–333, doi:10.1016/j.ijrmms.2009.09.012.

Shreve, R. L. (1968), Leakage and fluidization in air-layer lubricated avalanches, *Geol. Soc. Am. Bull.*, *79*(5), 653–658.

Stoopes, G. R., and M. F. Sheridan (1992), Giant debris avalanches from the Colima Volcanic Complex, Mexico: Implications for long-runout landslides (>100 km) and hazard assessment, *Geology*, *20*(4), 299–302.

Strom, A. (2006), Morphology and internal structure of rockslides and rock avalanches: Grounds and constraints for their modelling, in *Landslides From Massive Rock Slope Failure*, edited by S. G. Evan et al., pp. 305–326, Springer, Netherlands.

Strom, A. L. (1999), The morphology and internal structure of large rockslides as indicators of their formational mechanisms, *Dokl. Earth Sci.*, *369*(8), 1079–1081.

Taboada, A., and N. Estrada (2009), Rock-and-soil avalanches: Theory and simulation, *J. Geophys. Res.*, *114*, F04098, doi:10.1029/2008JF001072.

Thornton, C., K. K. Yin, and M. J. Adams (1996), Numerical simulation of the impact fracture and fragmentation of agglomerates, *J. Phys. D Appl. Phys.*, *29*(2), 424–435, doi:10.1088/0022-3727/29/2/021.

Utili, S., T. Zhao, and G. T. Houlsby (2015), 3D DEM investigation of granular column collapse: Evaluation of debris motion and its destructive power, *Eng. Geol.*, *186*(0), 3–16, doi:10.1016/j.enggeo.2014.08.018.

Wang, S., D. Elsworth, and J. Liu (2013), Mechanical behavior of methane infiltrated coal: The roles of gas desorption, stress level and loading rate, *Rock Mech. Rock Eng.*, *46*(5), 945–958, doi:10.1007/s00603-012-0324-0.

Wang, Y. (2009), A new algorithm to model the dynamics of 3-D bonded rigid bodies with rotations, *Acta Geotech.*, *4*(2), 117–127, doi:10.1007/s11440-008-0072-1.

Wang, Y. N., and F. Tonon (2011), Dynamic validation of a discrete element code in modeling rock fragmentation, *Int. J. Rock Mech. Min. Sci.*, *48*(4), 535–545, doi:10.1016/j.ijrmms.2011.02.003.

Wang, Y., S. Abe, S. Latham, and P. Mora (2006), Implementation of particle-scale rotation in the 3-D lattice solid model, *Pure Appl. Geophys.*, *163*(9), 1769–1785, doi:10.1007/s00024-006-0096-0.

Weatherley, D., V. Boros, and W. Hancock (2011), *ESyS-Particle Tutorial and User's Guide Version 2.1*, 153 pp., Earth Syst. Sci. Comput. Centre, The Univ. of Queensland, Brisbane, Australia.

Weibull, W. (1951), A statistical distribution function of wide applicability, *J. Appl. Mech.*, *18*, 293–297.

Whitehouse, I. E., and G. A. Griffiths (1983), Frequency and hazard of large rock avalanches in the central Southern Alps, New Zealand, *Geology*, *11*(6), 331–334.

Xu, Y., F. Dai, N. W. Xu, and T. Zhao (2016), Numerical investigation of dynamic rock fracture toughness determination using a semi-circular bend specimen in Split Hopkinson Pressure Bar testing, *Rock Mech. Rock Eng.*, *49*(3), 731–745, doi:10.1007/s00603-015-0787-x.

Yoon, J. (2007), Application of experimental design and optimization to PFC model calibration in uniaxial compression simulation, *Int. J. Rock Mech. Min. Sci.*, *44*(6), 871–889, doi:10.1016/j.ijrmms.2007.01.004.

Zhao, T., S. Utili, and G. B. Crosta (2016), Rockslide and impulse wave modelling in the Vajont reservoir by DEM-CFD analyses, *Rock Mech. Rock Eng.*, *49*(6), 2437–2456, doi:10.1007/s00603-015-0731-0.

Zhao, T., F. Dai, and N.-w. Xu (2017), Coupled DEM-CFD investigation on the formation of landslide dams in narrow rivers, *Landslides*, *14*(1), 189–201, doi:10.1007/s10346-015-0675-1.

Zhao, Y. X., S. M. Liu, G. F. Zhao, D. Elsworth, Y. D. Jiang, and J. L. Han (2014), Failure mechanisms in coal: Dependence on strain rate and microstructure, *J. Geophys. Res. Solid Earth*, *119*, 6924–6935, doi:10.1002/2014JB011198.

Zhou, J.-W., P. Cui, and H. Fang (2013), Dynamic process analysis for the formation of Yangjiagou landslide-dammed lake triggered by the Wenchuan earthquake, China, *Landslides*, *10*(3), 331–342, doi:10.1007/s10346-013-0387-3.